



HAL
open science

3D Curvature-Based Tip Load Estimation for Continuum Robots

Matyas Diezinger, Brahim Tamadazte, Guillaume Laurent

► **To cite this version:**

Matyas Diezinger, Brahim Tamadazte, Guillaume Laurent. 3D Curvature-Based Tip Load Estimation for Continuum Robots. *IEEE Robotics and Automation Letters*, 2022, 7 (4), pp.10526-10533. 10.1109/LRA.2022.3194680 . hal-04184144

HAL Id: hal-04184144

<https://hal.science/hal-04184144>

Submitted on 21 Aug 2023

HAL is a multi-disciplinary open access archive for the deposit and dissemination of scientific research documents, whether they are published or not. The documents may come from teaching and research institutions in France or abroad, or from public or private research centers.

L'archive ouverte pluridisciplinaire **HAL**, est destinée au dépôt et à la diffusion de documents scientifiques de niveau recherche, publiés ou non, émanant des établissements d'enseignement et de recherche français ou étrangers, des laboratoires publics ou privés.

3D curvature-based tip load estimation for continuum robots

Matyas Diezinger¹, Brahim Tamadazte², and Guillaume J. Laurent¹

Abstract—This paper presents a method intended for the estimation of external force and moment applied at the tip of thin continuum robots using vision-based shape measurements. A versatile vision process that does not require any additional markers nor sensors provides an accurate 3D reconstruction of the deformable rod shape. Then, the tip loads are directly deduced from the curvature along this curve formed by deformed rod thanks to the resolution of a linear system without requiring any iterative optimization. The curvature is determined with a robust method that allows filtering out measurement noise and artefacts. Simulations show that this approach gives fast and precise results in both 2D (planar forces estimation without torsion) and 3D (spatial forces estimation). Experimental results on cantilever rods show an accuracy of 2.2% and 2.7% of the applied forces and moments, respectively.

Keywords— Continuum robots, small-scale robots, force and moment estimation, stereo-vision, 3D reconstruction.

I. INTRODUCTION

Continuum Robots (CRs) have the potential to be used in a wide range applications, from medical to industrial. Unlike standard robots, CRs are made of slender flexible elements in place of rigid links. Numerous CRs have been proposed in the past few years [1], [2]. There is a common consensus that CRs offer several advantages over conventional architectures, e.g., their slender shapes as well as their potential to be miniaturized [3] allow them to reach thinly accessible area inside human bodies [2] or inside machines (turbine engines for instance). Indeed, the removal of mechanical joints allows to down size all the structure and to provide six Degrees of Freedom (DoF) with robots having diameters of a few millimeters [4], [5]. Additionally, the compliant nature of CRs confers safer interactions with humans for collaborative tasks in industry or for medical applications [6].

Conversely, the flexibility of CRs reduces the forces and moments that can be obtained at their end-effector. The payload of these robots is also much lower than their rigid counterpart. The most serious limitation is to guaranty the robot trajectory under different loads, i.e., under different applied external forces and moments. Traditional models of CRs are based on Cosserat rod theory [7], [8], [9] and allows calculating the actuators positions/angles to reach a desired pose in the Cartesian space. However, if the external loads

This work was supported by the French ANR program Spider (ANR-19-CE33-0002-02), Région de Bourgogne-Franche-Comté, Equipex ROBOTEX network (ANR-10-EQPX-44-01), and EUR EIPHI program (ANR-17-EURE-0002).

¹ M. Diezinger and G. Laurent are with FEMTO-ST Institute, Univ. Bourgogne Franche-Comté, CNRS, Besançon, France. matyas.diezinger@femto-st.fr, guillaume.laurent@ens2m.fr

² B. Tamadazte is with Sorbonne Université, CNRS UMR 7222, INSERM U1150, ISIR, F-75005, Paris, France. brahim.tamadazte@cnrs.fr

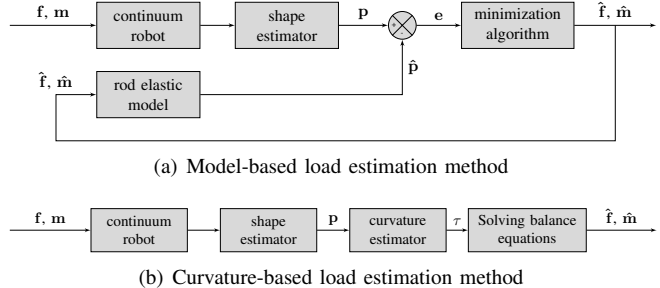


Fig. 1: Load estimation from shape (f , m , p , e are force, moment, position and position error vectors, respectively).

are not known, the models cannot predict the end-effector position. Indeed, the pose of CRs is highly dependent on unpredictable external interactions. This leads to a load-dependent trajectory that limits the capabilities of the robot. However, the compliant nature of CRs can also be used as an advantage during the design of a control strategy. As their deformations are the direct reflection of external forces, their shapes can be used to estimate these interactions. This approach has been investigated using different deformation sensors as Bragg fibers [10], [11], [12] or cable tension sensors [13].

Although the use of proprioceptive sensors can be the solution in certain configurations or applications, their integration on a CR is not straightforward, especially at small scale. Robots deformations are then more easily estimated by exteroceptive sensors. Among these are magnetic sensors [14], cameras [15], [16], x-ray imaging [17], optical-coherence tomography [18] as well as ultrasound imaging [19], [20]. Vision-based methods in particular are indeed less invasive but have also usually lower costs and a more flexible range of use.

Vision-based force estimation methods require first to estimate the deformation of the CR. Then, from the measured shape, the two usual ways of estimating external loads are model-based and curvature-based methods as shown in Fig. 1. Model-based methods are built on rod deformation models and iterative optimizations. The principle is to create a system-like model that predicts deformations from external guessed forces, and to make them converge by reducing errors between the simulated and the measured shapes. The model-based methods are usually based on the Cosserat theory [23], [12], [24], or on simpler piece-wise constant curvature models [25], [22] among others. However, these approaches are often slow because of model integration and iterative optimizations. They have also some difficulties to

TABLE I: Accuracy comparison of tip force estimation on cantilever rods and catheters (single planar bending).

Related work	Sensor	Method	Object dimensions (mm)	Mean relative error
Back et al. [21]	Vision	Curvature-based	L130 × Ø3	10% of applied magnitude
Hasanzadeh et al. [22]	CMM machine	Model-based	L70 × xØ2.33	11.4% of average magnitude
Khan et al. [10]	Bragg fibers	Curvature-based	L210 × Ø0.25	6.9% of applied magnitude
Aloi et al. [23]	Vision	Model-based	L200 × Ø1.4	6.7% of average magnitude
Hoosiar et al. [17]	Vision	Curvature-based	L40 × Ø6	7.5% of maximum magnitude
Al-Ahmad et al. [12]	Bragg fibers	Model-based	L170 × Ø2.16	5.5% of applied magnitude
Xiao et al. [11]	Bragg fibers	Curvature-based	L290 × Ø1.4	5.25% to 12.87% of applied magnitude
Proposed method	Stereo-vision	Curvature-based	L150 × Ø1	2.2% of applied magnitude

converge with 3D and large deformations because the inverse problem is often ill-conditioned [23].

On the contrary, curvature-based methods are not iterative and do not require the integration of any differential equations. They can provide more robust estimations with fast computation time. The concept is to find an estimator that links the measured shape straight to internal forces and moments (Fig. 1b). Then, the external loads are estimated by solving the balance of forces and moments in several points of the CR. Obviously, this method is perfectly adapted to CRs that embed Bragg fibers as illustrated in the recent work [11]. However, some studies has been also performed with vision-based shape estimation. For instance, in [21], the curvature-based estimation is applied with a continuum robot constrained in planar motion yielding an interesting result because the obtained estimation error is approximately 10% of the applied force. The same order of estimation error is reported in [17] using real-time x-ray imaging and Bézier curve smoothing.

Both methods require a precise and robust shape measurement method. One challenge to force estimation on CRs is the handling of three dimensional external forces. Most of the above-mentioned works deal with planar deformations and loads, generally yielding an external force estimation with error between 5% and 10% of the applied magnitude as reported in Table I. Additional methods dealing with 2.5D configurations (i.e., slightly extra-planar loads, but quasi-planar deformations) [10], [11] reported similar performances in term of accuracy and robustness. In fact, the tri-dimensional deformations lead to increased complexity in the force estimation for various reasons including: the challenging accurate reconstruction of the 3D deformations, the necessary estimation of the torsion, the ill-conditioning issues, etc. One of the most advanced works dealing with the estimation of 3D external forces is probably the one reported in [12] yielding an accuracy of approximately 5.5% using several Bragg fibers embedded along the CR.

In this paper, we set up an accurate and versatile 3D reconstruction method suitable for all shapes and sizes of thin continuum robots without any additional visual markers nor embedded sensors. Furthermore, we develop a curvature-based approach to estimate the 3D tip forces on a longitudinal deformable structure based on the direct measurement of its shape. Also, the proposed force estimation method is real-time and does not require any optimization method usually used for such problem whose performances depend directly on the proper conditioning of the optimizer. The developed

force estimation method allows to robustly filter out measurement noise and artefacts. One of the main advantages of the proposed method is the ability to work in 2D (planar forces estimation without torsion) and 3D (spatial forces estimation) configurations. Finally, the proposed method and material were successfully evaluated both numerically and experimentally.

The remainder of this paper is organised as follows. In Section II, we introduce the stereo-vision-based framework for 3D reconstruction of unknown shape rods. Section III presents the developed method for forces estimation on longitudinal deformable structure. The numerical validation of the proposed methods and materials is discussed in Section IV, when the experimental validations are discussed in Section V.

II. SHAPE RECONSTRUCTION OF RODS BY STEREOVISION

The first step of the proposed forces estimation approach consists of the shape reconstruction of the CR. Thus, this section deals with the tri-dimensional reconstruction of longitudinal deformable structures (e.g., rods) using a stereovision system and the epipolar geometry principles.

A. Epipolar Geometry

The stereovision system consists of a pair of standard cameras placed remotely in a manner to visualize the deformable structure with a given angle of view for each camera (Fig. 2). Therefore, the cameras provide a pair of images of a rod used to reconstruct a set of n measured 3D positions $\mathbf{p}(s_i)$ for $i = 1, \dots, n$ at arc length position s_i .

It can be noticed that most of continuum robots are made of uniform and monochrome materials (e.g., Nitinol, different types of polymers, silicon, etc.) which raises the problem of the lack of visible and recognizable visual features that can be easily and accurately detected, matched and tracked over time. By the way, although we want to add artificial markers, it is often difficult to integrate them on the continuum robot due to the size and the incompatibility with the targeted applications. Hence, we investigated a method for 3D reconstruction that does not requires visual markers or *a priori* knowledge of the viewed object. This method is based on the use of the well-established epipolar geometry principle [26] as well as image processing methods easy to set up and sufficiently robust and accurate with respect to the targeted applications.

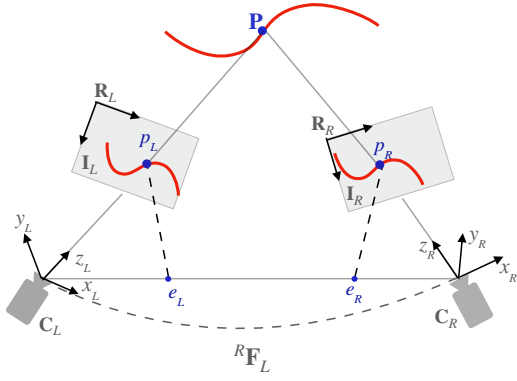


Fig. 2: Illustration of the built stereovision system used to reconstruct the 3D shape of a rod.

1) *Setup configuration and involved notations:* Starting with the introduction of the built stereovision system as well as the notations involved in the 3D reconstruction algorithm. Let us consider two cameras c_R and c_L with optical centers o_R and o_L view a 3D point $\mathbf{p} = (x, y, z)^\top$ which is projected in 2D image points $\mathbf{p}_L = (x_L, y_L)^\top$ and $\mathbf{p}_R = (x_R, y_R)^\top$. These two points are in the image planes \mathbf{I}_R and \mathbf{I}_L , respectively. The line $(o_R o_L)$ between both the camera optical centers defines the stereovision system baseline. The intersections of the baseline with the image planes give the so-called epipolar points (or epipoles) e_L and e_R , when the lines $(e_R p_R)$ and $(e_L p_L)$ are known as epipolar lines. Therefore, each 2D point \mathbf{p}_L in the left image is mathematically related to the epipolar line $(e_R p_R)$ in the right image and *vice-versa*.

The intrinsic parameters of both the right and the left cameras are defined with the matrices \mathbf{K}_R and \mathbf{K}_L , respectively. The extrinsic parameters that represents the pose of cameras in a common reference frame, which can be chosen as the left camera's frame \mathcal{R}_{C_L} , is defined as the 3D transformation ${}^R\mathbf{T}_L$ between the poses of camera c_R and camera c_L . This transformation includes a 3×3 rotation matrix ${}^R\mathbf{R}_L$ and a 3×1 translation vector ${}^R\mathbf{t}_L$.

2) *Epipolar projection model:* The relations between a world point \mathbf{p} and its two projections on the left and right images \mathbf{p}_i $i \in [R, L]$ can be expressed as follows for both the right and left cameras, respectively:

$$[\tilde{\mathbf{p}}_L]_{\times} \mathbf{K}_L [\mathbf{I}_{3 \times 3} \mid \mathbf{0}_{3 \times 1}] \tilde{\mathbf{p}} = \mathbf{0} \quad (1)$$

$$[\tilde{\mathbf{p}}_R]_{\times} \mathbf{K}_R [\mathbf{I}_{3 \times 3} \mid \mathbf{0}_{3 \times 1}] {}^R\mathbf{T}_L \tilde{\mathbf{p}} = \mathbf{0} \quad (2)$$

where $\mathbf{I}_{3 \times 3}$ is a 3×3 identity matrix, $\mathbf{0}_{3 \times 1}$ a 3×1 null-matrix, $\tilde{\mathbf{p}}_i = (\mathbf{p}_i, 1)^\top$ and $\tilde{\mathbf{p}} = (\mathbf{p}, 1)^\top$ are the homogeneous coordinates of \mathbf{p}_i and \mathbf{p} , respectively, and $[\]_{\times}$ is a 3×3 skew-symmetric matrix representing a vector cross-product.

Furthermore, note that both the camera intrinsic and extrinsic parameters are obtained using a well-known camera calibration toolbox [27].

3) *Rectification:* In order to simplify the problem of matching left and right image points, it is useful to perform a rectification procedure on the images in order to make the

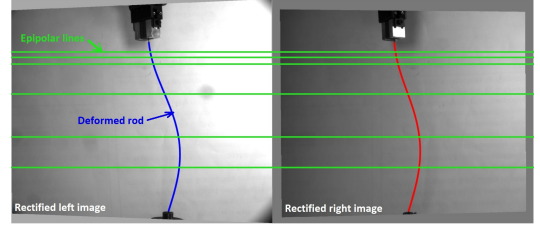


Fig. 3: Correlation process on rectified images of a rod.

epipolar lines, in both the right and left images, perfectly horizontal with respect to the respective images frames. This means that both e_R and e_L are located at infinity. Therefore, each point in the right image has its match in the left image along the same horizontal epipolar line, which makes the matching process much easier (Fig. 3).

4) *Correlation:* Once the rectification is done, it becomes trivial to determine and match the rod points between the right and left images. Both functions are performed using a conventional zero-mean normalized cross correlation (ZNCC) method [28]. With x, y defining an image reference frame in pixels, the correlation error is computed at fixed line x as following:

$$\epsilon(x_0, x) = \min_{\alpha, \beta} \frac{\sum_y |\alpha \mathbf{I}_{L_C}(x, y - \beta) \mathbf{I}_{L_C}(x_0, y)|^2}{\sum_y |\mathbf{I}_{L_C}(x_0, y)|^2} \quad (3)$$

where x_0 is the index of the first line crossing the rod, x is the current line index, α is the correlation coefficient and β is the transverse offset from which the disparity is computed.

Thereby, for each point \mathbf{p}_{iL} ($i = 1, \dots, n$) in the left rectified image \mathbf{I}_{L_C} , we search the corresponding point \mathbf{p}_{iR} in the right rectified image \mathbf{I}_{R_C} along the corresponding horizontal epipolar line to which the point belongs. Consequently, we obtain two coherent 2D curves representing the deformable structure in each image as can be seen in Fig. 3.

B. Triangulation

Now, we have all the ingredients to reconstruct the continuum robot geometry. The previous steps have led to two set of matched image-points \mathbf{p}_{iL} and \mathbf{p}_{iR} ($i = 1, \dots, n$), and an off-line estimation of both the intrinsic and the extrinsic parameters. Using these elements, the complete shape of the rod can be reconstructed using equations (1) rewritten as $\mathbf{A}_1 \tilde{\mathbf{p}} = 0$ and equation (2) rewritten as $\mathbf{A}_2 \tilde{\mathbf{p}} = 0$ combined as a unique equations system $\mathbf{A} \tilde{\mathbf{p}} = 0$ with $\mathbf{A} = \begin{bmatrix} \mathbf{A}_1 \\ \mathbf{A}_2 \end{bmatrix}$.

As reported in [26], the resolution of this system can be tackled by computing the eigenvectors. The solution is found using an singular value decomposition (SVD) of matrix \mathbf{A} , giving a good estimation of \mathbf{p} .

III. LOAD ESTIMATION FROM RODS SHAPES

With a view to the initial objective of estimating external loads on a continuum robot by measuring it thanks to a vision-based method, the following section aims at proceeding the computed deformations of a rod to determine the involved external tip forces and moments.

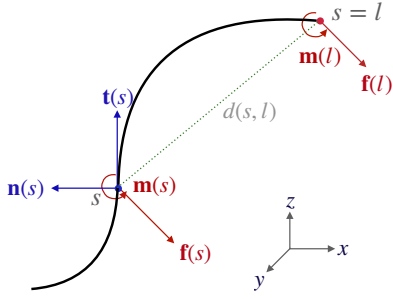


Fig. 4: Illustration of the balance between external force and moment.

A. Problem Statement

Continuum robots are slender actuated rods subjects to nonlinear deformations with proper mechanical properties. These properties as well as the initial straight configuration are known. We assume that no distributed forces or moments are applied along the rod except its own know gravity attraction. Punctual force and moment localized at rod tip are responsible for large shape deformations. The section dimension is negligible compared to length so that the rod is considered uni-dimensional. The shearing forces are then ignored compared to bending and twisting moments. Moreover, the material of the rod is taken linearly elastic and isotropic.

Let us consider a rod whose 3D shape is defined as a set of n measured 3D positions $\mathbf{p}(s_i)$ for $i = 1..n$ at arc length position s_i . Its proximal and distal ends are located at arc length 0 and l (Fig. 4), respectively. The rod is at static equilibrium, therefore the pose of each point of the rod is the image of the local moment due to external load forces.

B. Tip Force Estimation

The external force and moment are not measurable at a single point on a CR. But the 3D shape of the robot gives multiple images of the local moment due to external loads. The static equilibrium of the moments is relied upon to deduce these force and moment. The static state of the rod implies balanced moments and forces. Then, given a point of the rod located at the arc length position s , the moments applied to the portion $[s, l]$ are balanced at s :

$$\mathbf{m}(l) + \mathbf{d}(s, l) \times \mathbf{f}(l) + \mathbf{w}(s) - \mathbf{m}(s) = 0 \quad (4)$$

where $\mathbf{w}(s) = \int_s^l \mathbf{d}(s, u) \times \mathbf{g} \rho a du$ is the moment contribution induced by the mass of the rod portion $[s, l]$ and:

- a is the section of the rod;
- $\mathbf{d}(s, l)$ is the formed vector from point $\mathbf{p}(s)$ to point $\mathbf{p}(l)$;
- $\mathbf{f}(s)$ is the external force located at s ;
- \mathbf{g} is the local acceleration of free fall;
- $\mathbf{m}(s)$ is the external moment located at s ;
- ρ is the linear mass of the rod;

The unknown tip load is expressed in (4) by the rod-end moment $\mathbf{m}(l) = (m_x, m_y, m_z)^\top$ and force $\mathbf{f}(l) =$

$(f_x, f_y, f_z)^\top$ (Fig. 4). Note that each 3D reconstructed point $\mathbf{p} = (x, y, z)^\top$ of the rod yields three equations (one per axis), then at least two points are necessary to estimate the six unknowns of the tip load. However, for a better precision and robustness to measurement errors, it is highly recommended to consider a larger number of reconstructed 3D points. Thereby, (4) can be rewritten as a redundant linear system of equations in the form of $\mathbf{A}\mathbf{x} = \mathbf{y}$:

$$\underbrace{\begin{bmatrix} [\mathbf{d}(s_0, s_k)]_\times & \mathbf{I}_{3 \times 3} \\ \vdots & \vdots \\ [\mathbf{d}(s_n, s_k)]_\times & \mathbf{I}_{3 \times 3} \end{bmatrix}}_{\mathbf{A}} \cdot \underbrace{\begin{bmatrix} \mathbf{f}(l) \\ \mathbf{m}(l) \end{bmatrix}}_{\mathbf{x}} + \underbrace{\begin{bmatrix} \mathbf{w}(s_0) \\ \vdots \\ \mathbf{w}(s_n) \end{bmatrix}}_{-\mathbf{y}} - \underbrace{\begin{bmatrix} \mathbf{m}(s_0) \\ \vdots \\ \mathbf{m}(s_n) \end{bmatrix}}_{-\mathbf{y}} = 0 \quad (5)$$

To solve the system (5), a QR decomposition is used in order to transform the matrix \mathbf{A} , as product of an orthogonal matrix \mathbf{Q} and an upper triangular matrix \mathbf{R} (i.e., $\mathbf{A} = \mathbf{QR}$). Therefore, the problem can be tackled by a backwards substitution technique.

Building the system (5) requires a set of position points reconstructed with vision techniques, and a set of local moments that can be estimated from these positions as follows.

C. Local Moment Estimation

On a 3D curve, the local section orientation follows the deformations. Let that orientation be given by the Frenet-Serret frame formed at each position $\mathbf{p}(s)$ by the tangent unit vector $\mathbf{t}(s)$, the normal unit vector $\mathbf{n}(s)$, and the binormal unit vector $\mathbf{b}(s)$ obtained as the cross product of $\mathbf{t}(s)$ and $\mathbf{n}(s)$. The triplet of vectors are obtained as follows:

$$\mathbf{t}(s) = \frac{\mathbf{p}'(s)}{\|\mathbf{p}'(s)\|} \quad (6)$$

$$\mathbf{n}(s) = \frac{\mathbf{t}'(s)}{\|\mathbf{t}'(s)\|} \quad (7)$$

then,

$$\mathbf{b}(s) = \mathbf{t}(s) \times \mathbf{n}(s) \quad (8)$$

The rod deformations are given by the curvature κ and the torsion τ that represent the flexion and the twist, respectively. The curvature is the deviation of the tangent from a straight direction, locally following a circular arc. In other words, the inverse radius of this arc is the curvature. The plane containing this arc is named the osculating plane and contains by definition the tangent vector $\mathbf{t}(s)$ and the normal vector $\mathbf{n}(s)$. The torsion τ is the spatial speed of rotation of the osculating plane, i.e. the speed of rotation of its normal $\mathbf{b}(s)$. The curvature and the torsion are defined, respectively, as follows:

$$\kappa(s) = \|\mathbf{t}'(s)\| \quad (9)$$

$$\tau(s) = \|\mathbf{b}'(s)\| \quad (10)$$

The deformations are directly related to the local moments $\mathbf{m}(s)$ through stress-strain constitutive laws which are expressed as follows:

$$\mathbf{m}(s) = EI\kappa(s)\mathbf{b}(s) + GJ\tau(s)\mathbf{t}(s) \quad (11)$$

where E is the Young's modulus, I is the quadratic moment of area along radial direction, G is the shear modulus and J is the torsion constant (quadratic moment of area along axial direction).

D. Discrete Curvature and Torsion Estimation

The computation of the local moment uses the estimation of the tangent and binormal vectors as well as the curvature and torsion. All these elements can be defined from the positions $\mathbf{p}(s)$ and its three first derivatives [29]. However, even if the 3D reconstruction method for rod shape estimation is accurate, the deformation estimation is sensitive to measurement noise, especially emphasized by the use of derivatives. Indeed, the evaluation of discrete curvature and torsion from position is challenging and has been addressed in several ways such as B-spline smoothing [30] or weighted least-squares curve fitting [31].

To avoid the use of 3-order spatial derivatives, the curvature and the torsion can alternatively be estimated from the osculating plane and its rotation rates around the tangent vector as proposed by [32]. This method is more robust to measurement noise and its implementation is available for MATLAB¹. In order to tackle the induced measurement noise, the Frenet frame estimation is performed on a sliding window centered at each curvilinear abscissa s_i . The rod section taken in the sliding window is centered on the origin to form the point cloud \mathbf{P} defined as follows:

$$\mathbf{P}(s_i) = [\mathbf{p}(s_{i-k}) - \overline{\mathbf{p}(s_i)}, \dots, \mathbf{p}(s_{i+k}) - \overline{\mathbf{p}(s_i)}] \quad (12)$$

where $\overline{\mathbf{p}(s_i)}$ is the centroid of positions neighbouring $\mathbf{p}(s_i)$.

The eigenvectors of the matrix $\mathbf{P}(s_i)$ form a frame attached to the estimated set of points. These are estimated with a singular value decomposition showed in equation (13). $\mathbf{U}(s_i)$ and $\mathbf{V}(s_i)$ are projective matrices and $\mathbf{D}(s_i)$ is the diagonal matrix containing the eigenvalues. The eigenvectors are the columns of $\mathbf{U}(s_i)$ and the tangent $\mathbf{t}(s_i)$ is given by the vector with greatest eigenvalue, as in a usual line correlation. The second greatest value gives the estimation of the normal $\mathbf{n}(s_i)$, and the third the estimation of the binormal $\mathbf{b}(s_i)$.

$$\mathbf{P}(s_i) = \mathbf{U}(s_i)\mathbf{D}(s_i)\mathbf{V}(s_i)^\top \quad (13)$$

The tangent and normal vectors $\mathbf{t}(s_i)$ and $\mathbf{n}(s_i)$ define the osculating plane at s_i . The curvature $\kappa(s_i)$ is then determined as the inverse of the radius of the best fitted circle in the osculating plane using the Taubin's method [33].

The torsion $\tau(s_i)$ corresponds to the rotation rate of the osculating plane. As the rotation of the osculating plane is continuous, the angle between consecutive normal vectors remains small but can be either positive or negative. Therefore the torsion is computed using the normal and the binormal at the previous position by:

$$\tau(s_i) = \frac{\arcsin(\mathbf{b}(s_{i-1}) \cdot \mathbf{n}(s_i))}{s_i - s_{i-1}} \quad (14)$$

¹https://de.mathworks.com/matlabcentral/fileexchange/47885-frenet_robust-zip

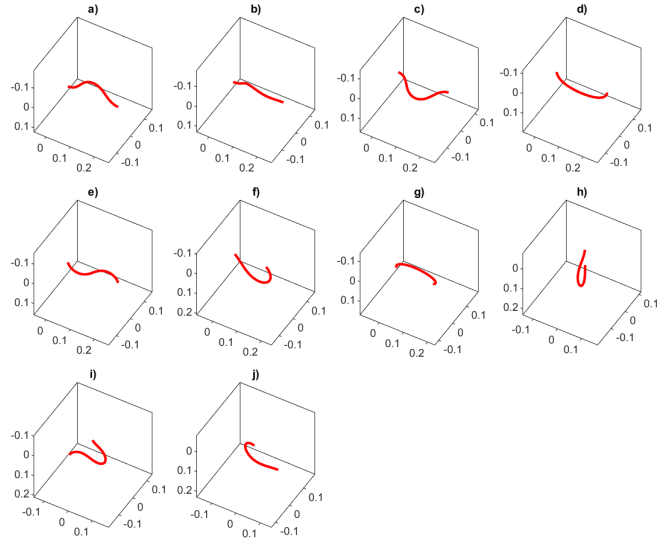


Fig. 5: Examples of simulated rods with given density ($2000\text{kg}\cdot\text{m}^{-3}$), young modulus (81GPa), shear modulus (32GPa), radius (0.5mm), length (260mm) and number of points (50).

The continuity of the normal and the binormal directions is ensured by avoiding flips that can occur on parts of the rod with zero curvature. Therefore, the normal vector does not always points toward the center of the osculating circle, that results in a negative curvature.

IV. NUMERICAL VALIDATION

The validation of the tip force estimation method goes through the evaluation of various 3D rods. To do this, it is necessary to numerically generate a data-set of different shaped rods. Also, the simulated rods allow evaluating all the state variables, particularly the internal moments.

The generation of several theoretical rod shapes is carried out with the robust finite element modeler available within the open-source simulation framework SOFA dealing with finite element modelling of deformable objects [34], [35]. Several 3D rod shapes are generated (Fig. 5) to cover different possible rod deflection shapes.

The proposed force estimation method was then evaluated on the different 3D obtained shapes depicted in Fig. 5. The estimated forces and moments are compared to the theoretical ones as can be seen in Fig. 6. The force estimation gives an average error of 0.062N (respectively, a maximum error of 0.26N) within a range of 2.6N, while the moment estimation gives an average error of 0.0044N.m (respectively, a maximum error of 0.0068N.m) within a range of 0.13N.m.

V. EXPERIMENTAL VALIDATION

A. Shape Reconstruction Validation

1) *Vision setup*: The vision shape estimator is built from two cameras placed at the same distance from a targeted rod, with a slightly different orientation and position as shown in Fig. 7. The rod to be reconstructed is fixed at the front of a

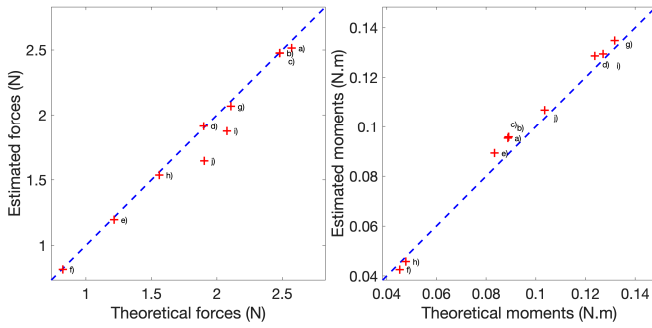


Fig. 6: Comparison of estimated tip force and moment with theoretical ground values for the ten simulated rods presented in Fig. 5.

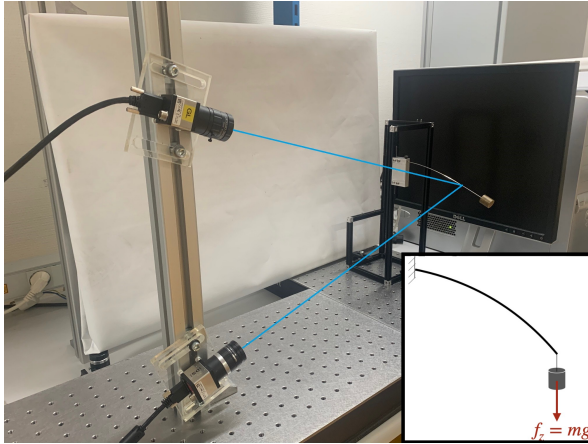


Fig. 7: Vision setup with cantilever rod.

black screen and enlightened in order to increase the contrast between the rod and the background more suitable for the correlation-based matching method.

2) *Shape estimation*: The 3D reconstruction process has been tested on single rods with various 3D shapes. Figure 8 shows several examples of reconstruction of different bent and twisted wires compared to the real ones. The experimental conditions being variable, some adaptive parameters are added to the process in order to make it more versatile. Among these, a coefficient for brightness, an upper boundary for rod diameter detection and the maximum allowed correlation shift. Allowing the user to change these parameters has made the process more robust and the shapes are then precisely reproduced for rods of several materials (steel, glass and plastic) whose diameter varies from 0.25mm to 2mm.

B. Model Validation

In order to verify the model, an experiment is conducted with a carbon fiber beam deformed to 4 different shapes with known tip orientation and position. The principal parameters are determined experimentally, the radius (0.5mm) is measured with a calliper, the density ($3032\text{kg}\cdot\text{m}^{-3}$) is measured with a precision balance and the young modulus (60GPa) and shear modulus (24GPa) are estimated with a 3-point flexure test. The shape is reconstructed by vision and

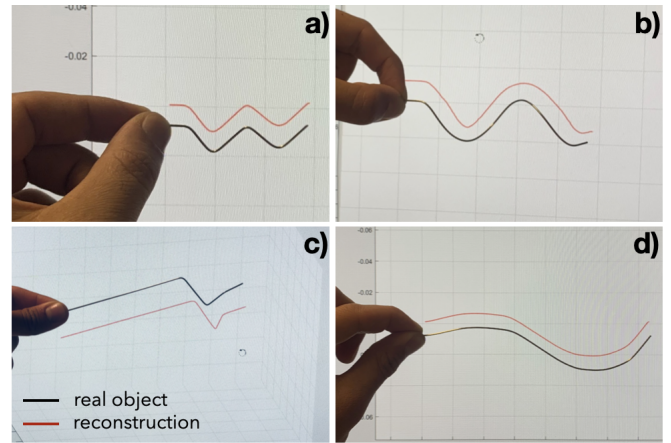


Fig. 8: Four examples of 3D shape reconstruction of bent and twisted wires.

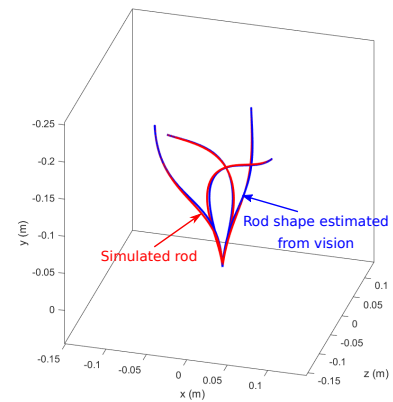


Fig. 9: Rods simulated from real rod end poses.

compared to a theoretical rod shape generated obtained with SOFA from the same parameters (Fig. 9). This validates the coherence and the reliability of both the vision process and the measured rod parameters used for the generated model. Note there is a minor shift between the reconstructed rods and the simulated ones. Two potential origins of error are envisaged: 1) the existence of an initial curvature/stress (not be taken into account in the model) when the rod is initially considered perfectly straight and 2) small lateral errors in the correlation process on rectified images, due to the acquisition conditions (blur, shadow). However, these shifts between 3D real shapes and reconstructed ones remain insignificant to actually impact the accuracy of the proposed force estimation method.

C. Moments Estimation

In order to validate experimentally the proposed force estimation method, we used a 150mm long steel cantilever rod (as depicted in Fig. 7) whose 3D shape has been reconstructed by the vision method. As mentioned in Section III-D, the efficiency and accuracy of the estimation of local curvature and torsion and then the local moments depend directly

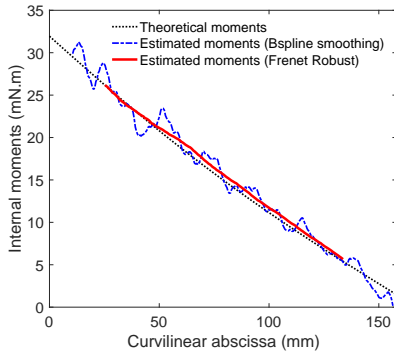


Fig. 10: Comparison of estimated internal moments magnitude in a cantilever rod.

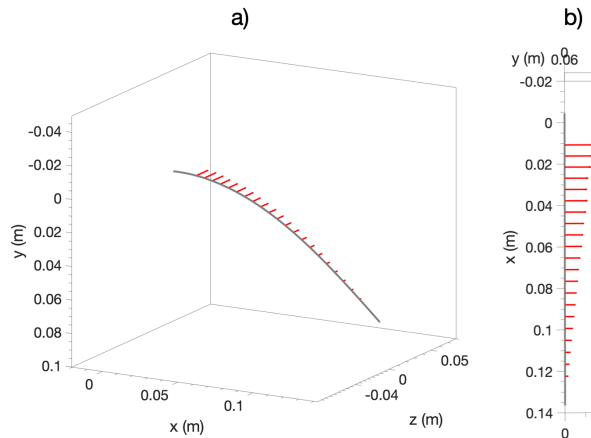


Fig. 11: a) Perspective view of the shape reconstruction of a cantilever rod with estimated internal moments, and b) a top view of the estimated internal moments.

on the ability to handle noise in position measurements. To highlight this, a comparison is made between Frenet bases estimated 1) from derivatives of positions after a B-Spline smoothing and 2) from the fitting of the osculating plane and circle (Frenet robust).

The rod is weighted with a 0.24N load at its end so that the deformations remain planar and there is no torsion involved. The moments are then all pointing to the same direction with decreasing magnitude. As shown in Fig. 10, the proposed method gives a more accurate estimation of the moments with an average error of 0.54mN.m and a maximum error of 0.99mN.m whereas the B-Spline smoothing method gives an average error of 1.47mN.m and a maximum error of 3.02mN.m. The local moments are represented on the reconstructed rod shape in Fig. 11.

D. Load Estimation on Cantilever Rods

The previous experiment has been conducted on five cantilever rods loaded with several masses from 12.8g to 35.48g in order to validate the accuracy of the method over a large range of loads. The measured parameters are the density ($3032\text{kg}\cdot\text{m}^{-3}$), the young modulus (60GPa), the shear modulus (24GPa) and the radius (0.5mm). The vision process gives the length of the rod (158mm).

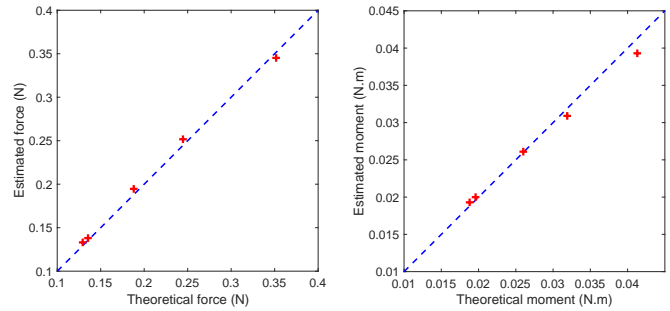


Fig. 12: Tip force and moment estimation errors on cantilever rods.

The forces due to the hanged weight are known and compared to the estimated forces, as shown in Fig. 12. The resulting errors are 2.2% on average of the applied forces when are 2.7% of applied moments, with maximum errors of 4.4% and 5.1%, respectively. It can be highlighted that the proposed method outperforms the state-of-the-art methods as can be seen in Table I. Note that, the more relevant method reported in the literature stated an accuracy of approximately 5.5% using Bragg fibers as means for the rod shape reconstruction.

E. Load Estimation from 3D Deformation

The force estimation tool developed in this paper has been tested on a rod deformed by hand to show applied force magnitude and direction at any time. Fig. 13 shows different rod deformations with the corresponding force and moment estimations in overlays. These experiments can be much more appreciate on the supplementary video file. These experiments illustrate the robustness of the proposed method to detect, to reconstruct and to estimate tip load in real conditions and paves the way to the force sensing/control of continuum robots.

VI. CONCLUSION

In this paper, an accurate and fast method to estimate tip loads on a continuum rod based on curvature calculation has been presented. Magnitude and direction are estimated for both external forces and moments from stereo images. Simulations on various rods with large deformations showed a precision of 0.062N within a range of 2.6N in the force measurement and experimental results on cantilever rods showed an accuracy of 2.2% of applied magnitude. The method can be applied to any 3D deformations of a rod without additional visual markers nor embedded sensors. In future work, we aim to implement this method for the force/position control of a parallel continuum robot. We also intend to use this method as an adaptive haptic feedback sensor.

REFERENCES

- [1] R. J. Webster III and B. A. Jones, "Design and kinematic modeling of constant curvature continuum robots: A review," *The Int. J. of Rob. Res.*, vol. 29, no. 13, pp. 1661–1683, 2010.

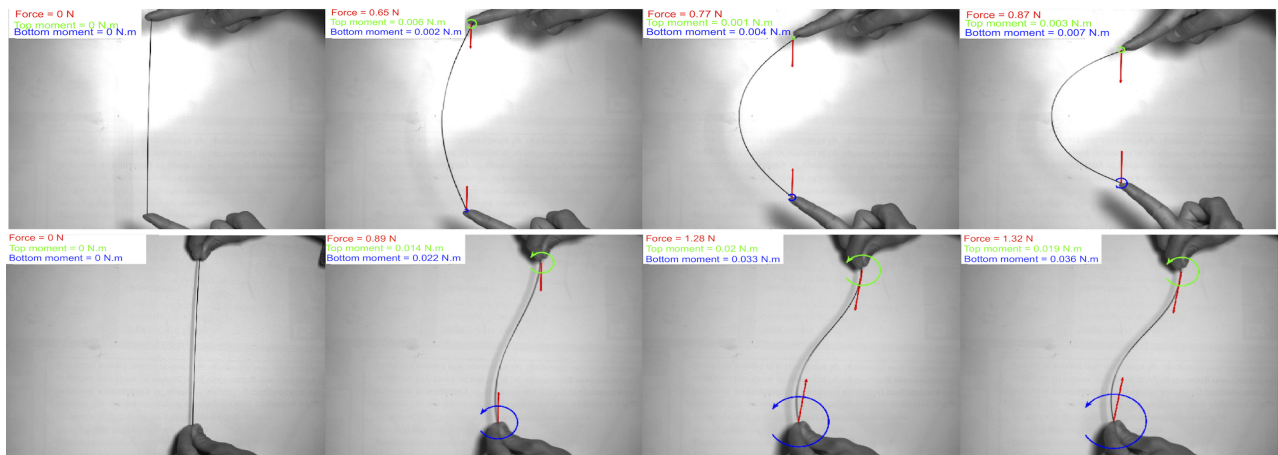


Fig. 13: Estimated forces and moments on "C-shape" rod (first row) and "S-shape" rod (second row). Additional examples can be seen in the attached multimedia materials.

- [2] J. Burgner-Kahrs, D. C. Rucker, and H. Choset, "Continuum Robots for Medical Applications: A Survey," *IEEE T. on Rob.*, vol. 31, pp. 1261 – 1280, 2015.
- [3] X. Dong, D. Axinte, D. Palmer, *et al.*, "Development of a slender continuum robotic system for on-wing inspection/repair of gas turbine engines," *Rob. and Comp.-Integ. Manuf.*, vol. 44, pp. 218–229, 2017.
- [4] R. E. Goldman, A. Bajo, L. S. MacLachlan, *et al.*, "Design and performance evaluation of a minimally invasive telerobotic platform for transurethral surveillance and intervention," *IEEE T. on Biomed. Eng.*, vol. 60, pp. 918–925, 2013.
- [5] Y. Chitalia, N. J. Deaton, S. Jeong, *et al.*, "Towards fbg-based shape sensing for micro-scale and meso-scale continuum robots with large deflection," *IEEE Rob. and Auto. Let.*, pp. 1712–1719, 2020.
- [6] S. Sanan and C. G. Atkeson, "Continuum robots: An approach to safer robots," in *CiteSeer*, 2010.
- [7] S. S. Antman, *Nonlinear Problems of Elasticity*, 2nd ed., ser. Mathematics Subject Classification, 2005, vol. 107.
- [8] B. A. Jones, R. L. Gray, and K. Turlapati, "Three Dimensional Statics for Continuum Robotics," *Int. Conf. on Intel. Rob. and Syst.*, 2009.
- [9] D. C. Rucker, B. A. Jones, and R. J. Webster, "Statics and Dynamics of Continuum Robots With General Tendon Routing and External Loading," *IEEE T. On Rob.*, vol. 27, pp. 1033 – 1044, 2011.
- [10] F. Khan, R. J. Roesthuis, and S. Misra, "Force sensing in continuum manipulators using fiber bragg grating sensors," in *IEEE/RSJ Int. Conf. on Intel. Rob. and Syst.*, 2017, pp. 2531–2536.
- [11] Q. Xiao and Y. Chen, "Efficient force estimation for continuum robot," *arXiv preprint arXiv:2109.12469*, 2021.
- [12] O. Al-Ahmad, M. Ourak, J. Vlekken, and E. Vander Poorten, "Fbg-based estimation of external forces along flexible instrument bodies," *Frontiers in Robotics and AI*, vol. 8, 2021.
- [13] M. Jolaei, A. Hooshiar, A. Sayadi, *et al.*, "Sensor-free force control of tendon-driven ablation catheters through position control and contact modeling," in *Ann. Int. Conf. of the IEEE Eng. in Med. and Biol. Soc.*, 2020, pp. 5248–5251.
- [14] H. Guo, F. Ju, Y. Cao, *et al.*, "Continuum robot shape estimation using permanent magnets and magnetic sensors," *Sens. and Actua. A: Physical*, vol. 285, pp. 519–530, 2019.
- [15] D. B. Camarillo, K. E. Loewke, C. R. Carlson, *et al.*, "Vision based 3-D shape sensing of flexible manipulators," *IEEE Int. Conf. on Rob. and Auto.*, 2008.
- [16] J. M. Croom, D. C. Rucker, J. M. Romano, and R. J. Webster, "Visual Sensing of Continuum Robot Shape Using Self-Organizing Maps," *IEEE Int. Conf. on Rob. and Auto.*, 2010.
- [17] A. Hooshiar, A. Sayadi, M. Jolaei, and J. Dargahi, "Accurate estimation of tip force on tendon-driven catheters using inverse cosserat rod model," in *Int. Conf. on Biom. Innov. and Appl.*, 2020, pp. 37–40.
- [18] Y. Baran, K. Rabenorosoa, G. J. Laurent, P. Rougeot, N. Andreff, and B. Tamadazte, "Preliminary results on oct-based position control of a concentric tube robot," in *IEEE/RSJ Int. Conf. on Intel. Rob. and Sys.*, 2017, pp. 3000–3005.
- [19] H. Ren, N. V. Vasilyev, and P. E. Dupont, "Detection of curved robots using 3d ultrasound," *IEEE/RSJ Int. Conf. on Intel. Rob. and Sys.*, pp. 2083–2089, 2011.
- [20] M. Aggravi, D. A. L. Estima, A. Krupa, *et al.*, "Haptic teleoperation of flexible needles combining 3d ultrasound guidance and needle tip force feedback," *IEEE Rob. and Auto. Let.*, pp. 4859–4866, 2021.
- [21] J. Back, T. Manwell, R. Karim, *et al.*, "Catheter Contact Force Estimation from Shape Detection using a Real-Time Cosserat Rod Model," *IEEE/RSJ Int. Conf. on Intel. Rob. and Sys.*, 2015.
- [22] S. Hasanzadeh and F. Janabi-Sharifi, "Model-based force estimation for intracardiac catheters," *IEEE/ASME T. on Mech.*, vol. 21, pp. 154–162, 2016.
- [23] V. A. Aloï and D. C. Rucker, "Estimating Loads Along Elastic Rods," *Int. Conf. on Rob. and Auto.*, 2019.
- [24] D. C. Rucker and R. J. Webster, "Deflection-Based Force Sensing for Continuum Robots: A Probabilistic Approach," *IEEE/RSJ Int. Conf. on Intel. Rob. and Sys.*, 2011.
- [25] M. Khoshnam, A. C. Skanes, and R. V. Patel, "Modeling and estimation of tip contact force for steerable ablation catheters," *IEEE T. on Biom. Eng.*, vol. 62, pp. 1404–1415, 2015.
- [26] R. Hartley and A. Zisserman, *Multiple View Geometry in Computer Vision*, 2nd ed. Cambridge University Press, 2000.
- [27] Z. Zhang, J. Dequidt, and C. Duriez, "Vision-Based Sensing of External Forces Acting on Soft Robots Using Finite Element Method," *IEEE Rob. And Auto. Let.*, 2018.
- [28] M. Guizar-Sicairos, S. T. Thurman, and J. R. Fienup, "Efficient subpixel image registration algorithms," *Opt. Lett.*, vol. 33, no. 2, pp. 156–158, 2008.
- [29] A. Pressley, "How much does a curve curve," in *Elementary Differential Geometry*, 2nd ed. Springer Undergraduate Mathematics Series, 2001, pp. 29–54.
- [30] N. Kehtarnavaz and R. Defigueiredo, "A 3-d contour segmentation scheme based on curvature and torsion," *IEEE T. on Pat. Anal. and Mach. Intel.*, vol. 10, pp. 707–713, 1988.
- [31] T. Lewiner, J. D. Gomes, H. Lopes, and M. Craizer, "Curvature and torsion estimators based on parametric curve fitting," *Computers and Graphics*, vol. 29, no. 5, pp. 641–655, 2005.
- [32] A. Gong, S. Rode, G. Gompper, *et al.*, "Reconstruction of the three-dimensional beat pattern underlying swimming behaviors of sperm," *The Eu. Phys. J. E*, vol. 44, p. 87, 2021.
- [33] G. Taubin, "Estimation of planar curves, surfaces, and nonplanar space curves defined by implicit equations with applications to edge and range image segmentation," *IEEE T. on Pat. Anal. & Mach. Intel.*, vol. 13, pp. 1115–1138, 1991.
- [34] F. Faure, C. Duriez, H. Delingette, *et al.*, "SOFA: A Multi-Model Framework for Interactive Physical Simulation," in *Soft Tissue Biomechanical Modeling for Computer Assisted Surgery*, 2012, pp. 283–321.
- [35] E. Coevoet, T. Morales-Bieze, F. Largilliere, *et al.*, "Software toolkit for modeling, simulation and control of soft robots," *Advanced Robotics*, vol. 31, pp. 1208–1224, 2017.